ACS Photonics

Article

pubs.acs.org/journal/apchd5

Testbeds for Transition Metal Dichalcogenide Photonics: Efficacy of Light Emission Enhancement in Monomer vs Dimer Nanoscale Antennae

Mohammad H. Tahersima,*[,†] M. Danang Birowosuto,[§] Zhizhen Ma,[†] William C. Coley,[‡] Michael D. Valentin,[‡] Sahar Naghibi Alvillar,[‡] I-Hsi Lu,[‡] Yao Zhou,[∥] Ibrahim Sarpkaya,[†] Aimee Martinez,[‡] Ingrid Liao,[‡] Brandon N. Davis,[‡] Joseph Martinez,[‡] Dominic Martinez-Ta,[‡] Alison Guan,[‡] Ariana E. Nguyen,[‡] Ke Liu,[†] Cesare Soci,[§] Evan Reed,[∥] Ludwig Bartels,[‡] and Volker J. Sorger[†]

[†]Department of Electrical and Computer Engineering, George Washington University, 800 22nd Street NW, Washington, DC 20052, United States

[‡]Chemistry and Materials Science & Engineering, University of California, Riverside, Riverside, California 92521, United States

[§]Division of Physics and Applied Physics, Nanyang Technological University, 21 Nanyang Link, Singapore 637371, Singapore

[∥]Department of Materials Science and Engineering, Stanford University, Stanford, California 94305, United States

Supporting Information

ABSTRACT: Monolayer transition metal dichalcogenides (TMDs) are materials with unique potential for photonic and optoelectronic applications. They offer well-defined tunable direct band gaps in a broad electromagnetic spectral range. The small optical path across them naturally limits the light−matter interactions of these two-dimensional (2-D) materials, due to their atomic thinness. Nanoscale plasmonic antennae offer a substantial increase of field strength over very short distances, comparable to the native thickness of the TMD. For instance, it has been demonstrated that plasmonic dimer antennae generate hot-spot field enhancements by orders of magnitude when an emitter is positioned exactly over the middle of their gap. However, 2-D materials cannot be grown or easily transferred, to reside midgap of the metallic dimer cavity. Hence, it is not plausible to simply take the peak intensity as the emission enhancement factor. Here we show that the emission enhancement generated in a 2-D TMD film by a monomer antenna cavity rivals that of dimer cavities at a reduced lithographic effort. We rationalize this finding by showing that the emission enhancement in dimer antennae depends not on the peak of the field enhancement at the center of the cavity but rather from the average field enhancement across a plane located beneath the optical cavity where the emitting 2-D film is present. We test multiple dimer and monomer antenna geometries and observe a representative 3-fold emission enhancement for both monomer and dimer cavities as compared to the intrinsic emission of chemical vapor deposition (CVD)-synthesized WS_2 flakes. This finding suggests facile control and enhancement of the photoluminescence yield of 2-D materials based on engineering of light−matter interactions that can serve as a testbed for their rapid and detailed optical characterization.

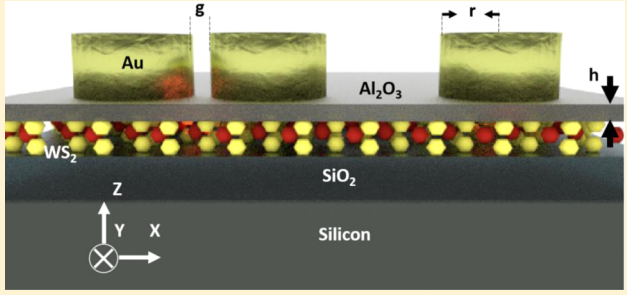

KEYWORDS: *optical antenna, light emitter, plasmonic, florescence, 2D materials, WS_2*

Nanoscale on-chip light-emitting structures are desired for a broad range of applications including displays, sensors, and optical interconnects. Transition metal dichalcogenides (TMDs) are two-dimensional (2-D) materials that show photoluminescence in the visible optical spectrum due to the emergence of a direct band gap at the K point in the Brillouin zone. They also offer the potential for high-quantum-yield emission and pure excitonic states.[1−4] TMDs are attractive materials for novel nanoscale optical emitters and optoelectronic devices.[5−11]

The structural, chemical, and electronically similar monolayer semiconducting TMDs MoS_2, $MoSe_2$, WS_2, and WSe_2 provide light emission in the visible and near-infrared spectral regions (1.1−2.0 eV).[1−4] The spatial confinement of carriers to a three-atom-thin physical plane and the weak dielectric screening in atomically thin materials lead to high oscillator strengths and strong Coulombic interactions between the excited electron−hole pairs. This results in strong binding energie,s allowing for observation of excitons at room temperature.[11−18] In addition to neutral excitons, charged trions can also be excited in the presence of residual excess charge carriers. These quasi particles consist either of two electrons and one hole (A^-) or one electron and two holes (A^+). Therefore, electrostatic gating

Received: March 3, 2017
Published: June 14, 2017

DOI: 10.1021/acsphotonics.7b00208
ACS Photonics 2017, 4, 1713−1721

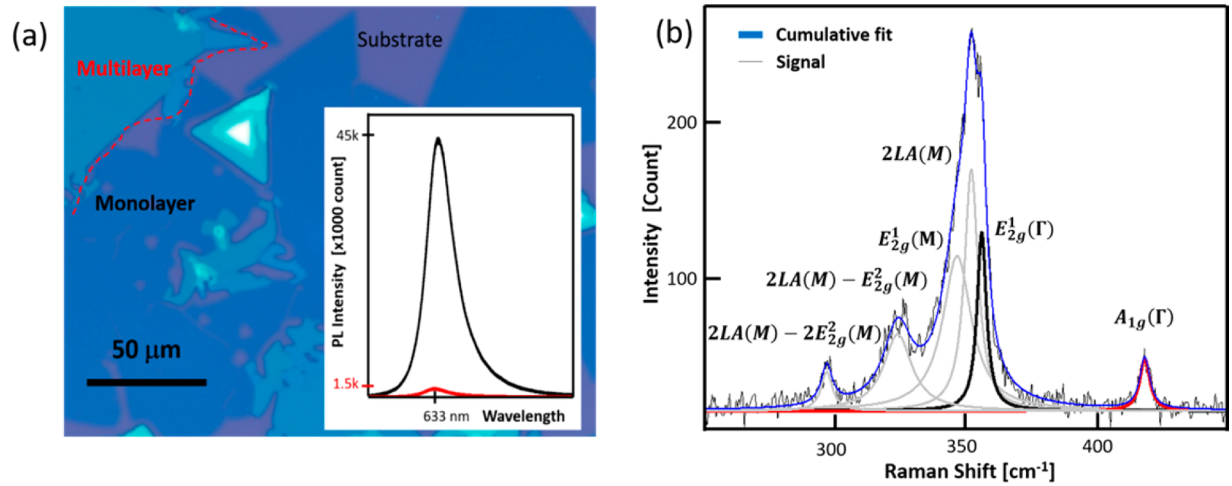

Figure 1. Optical characterization of CVD-grown WS_2 at room temperature. (a) Optical images of as-grown WS_2 on 100 nm SiO_2 on a silicon substrate. (Inset) Comparison of PL emission of monolayer and multilayer WS_2. (b) Room-temperature Raman spectra from a monolayer WS_2 flake, including Lorentzian peak fits for the 532 nm laser excitation.

modifies the spectral weight of charge-neutral excitonic species in TMDs.[14−17] Moreover, given the large binding energy of the excitons, the formation of states consisting of two excitons (biexciton) is possible in TMDs, whose photoluminescence (PL) emission is red-shifted due to the additional binding energy.[14,18,19]

A drawback of using TMD materials for photonic and optoelectronic applications is the low modal overlap with any externally applied optical field because of the atomic thickness of the monolayer material and the fundamentally weak light−matter interaction of bosons with fermions. Different strategies to tailor light−matter interaction and enhance both absorption and emission of these materials have been developed such as resonant (cavity, surface-plasmon resonance) and nonresonant (waveguide dispersion, metamaterials, index tuning) systems and were utilized to achieve maximum light absorption and emission.[20−35,40] Plasmonic nanoantennae fall into the former category, and they can synergistically (a) increase the absorption cross-section, thereby enhancing the pump efficiency, (b) accelerate the internal emission rate via the Purcell effect through the nanoscale optical mode of the antenna, and (c) improve emission out-coupling to free space via impedance matching (transformer action). As such, optical antennae increase the excitation rate while simultaneously enhancing the local density of states (DOS) in the emission process, which modifies (here accelerates) the spontaneous emission rate known as the Purcell effect.[25] Hence, these optical antennae behave as electromagnetic cavities that strongly modify spontaneous emission of fluorescence in the spatial and spectral proximity. Plasmonic antennae are unique cavities; a good antenna has a low quality (Q)-factor and is, thus, an effective radiator. However, the light−matter interaction enhancement quantifier is proportional to the ratio of Q/V, where V is the optical mode volume. Given the possibility for subdiffraction-limited plasmonic optical mode volumes, the inherently low Q-factors ensure a decent antenna function, while high Purcell factors of ∼10's to 100's are obtainable.[27,37,38] Compared to photonic high-Q cavities, plasmonic antennae allow for simultaneous high absorption and PL emission, if quenching is prevented. Antenna-enhanced light emitters have short radiative lifetimes and can have a deep subwavelength optical mode, thus opening the possibility of creating ultrafast, nanoscale emitters.[26]

Recently, multiple TMD−plasmonic hybrid nanostructures have been investigated.[27−35] However, a detailed study probing the actual origin of light emission enhancement in these hybrid nanostructures has not yet been reported. A common claim in previous studies is that the gap mode of the plasmonic dimer's field enhancement enables high Purcell factors. Plasmonic dimers, which are nanoscale structures consisting of two metallic nanoparticles separated by a small gap, support hybridized plasmon resonances because of the capacitive coupling between the plasmon modes of each nanoparticle. For a quantum emitter (e.g., <20 nm quantum dot) placed inside this gap, the coupling strongly localizes charges at the junction between the two nanoparticles, giving rise to large field enhancements at the center of the feed gap of the dimer antenna. However, for emitters that are not comparable in size to a quantum dot in all three dimensions, such as TMD films, the emitter must be offset from the antenna either below or on top of the antenna and, thus, is unable to take advantage of the highest electromagnetic field enhancement at the hot-spot. For TMD emitters with zero distance from the plasmonic antennae, the strong field gradients of the point dipole source can efficiently excite lossy multipolar modes of the antenna, which are mostly dark or weakly coupled to the radiation field and, therefore, convert the electromagnetic energy mostly into heat.[34] To prevent the emitter from being quenched (i.e., coupling to lossy plasmonic surface waves), the emitter should be separated from the metallic nanoparticle by a distance previously reported to be about ∼8 to 10 nm.[36−39] Before we fabricated TMD−nanocavity systems, we modeled a broad spectrum of dimer and monomer antenna configurations and find that—within the limitations imposed by the 2-D geometry of the film and the need for a separator—the maximum field enhancement of a dimer antenna relative to a monomer disc is only about 2-fold. For such designs, we observe that the pertinent cavity field enhancement in the dimer case does not originate from the gap between the metal particles, but from each monomer disc. We then further compare the TMD emission enhancement of monomer vs dimer antennae relative to intrinsic PL emission.

DOI: 10.1021/acsphotonics.7b00208
ACS Photonics 2017, 4, 1713−1721

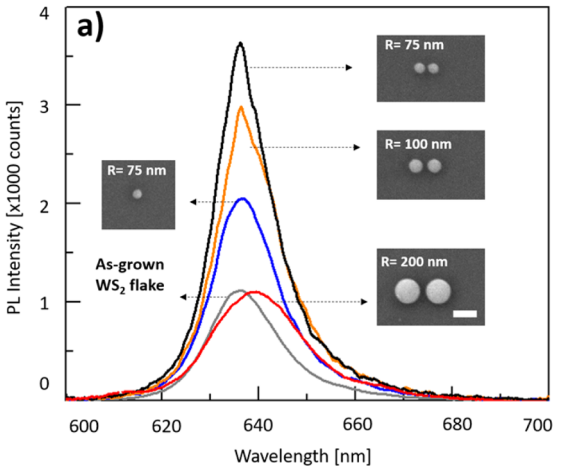

b)

Sample	FWHM	Σ PL / Σ PL⁰
Flake	16.7	1.0
200 nm r dimer	21.8	1.3
100 nm r dimer	13.5	2.4
75 nm r dimer	14.6	2.7
75 nm r monomer	15.7	1.8

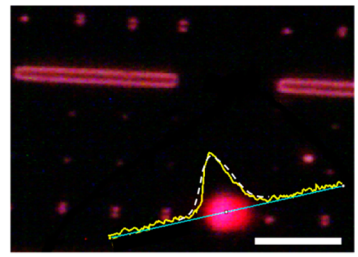

Figure 2. Collected photoluminescence (PL) emission from monolayer WS_2 is enhanced when it is placed under a plasmonic monomer or dimer antenna cavity with a resonance close to that of the emission wavelength. Electron beam lithography (EBL) has been used for fine-tuning of the optical antenna dimensions on the scale of 10's of nanometers (see Methods). (a) PL intensity of CVD-grown monolayer WS_2 before and after fabrication of four different optical antennae. Insets are SEM images of each type of optical cavity; the scale bar is 400 nm. (b) Full width at half-maxima (fwhm) and enhancement of integrated PL emission from the as-grown sample and for each optical antenna. (c) Dark-field optical image of the 637 nm PL emission from a monolayer WS_2 under an optical excitation of 532 nm. Fitting the beam intensity profile shows that 90% of the Gaussian beam power is within an 800 nm beam spot size. White scale bar = 5 μm.

Our work uses WS_2 single-layer islands prepared by chemical vapor deposition (CVD). CVD offers an, in principle, scalable source of TMD material for future technological implementation of this approach.[45] Prior work[27,30,33] on plasmonic antennae utilized material obtained through exfoliation. The CVD process is the preferred method for synthesizing TMD materials due to the pristine monolayer quality of the materials including a high level of process control as readily demonstrated by the semiconductor industry.

Although in atomically thin layered TMDs, atoms are confined in a plane, the electric field originating from dipole charges in the 2-D crystals has both in-plane and out-of-plane components. Moreover, the large surface to volume ratio in 2-D materials enhances the significance of surface interactions and charging effects. Thus, the dielectric permittivity mismatch between the 2-D semiconductor film, the surrounding environment, and an induced strain from capping material can intricately affect the electronic and optoelectronic properties of low-dimensional materials.[41]

In this study, we demonstrate that spontaneous emission of an atomically thin WS_2 film coupled to four different plasmonic nanocavity designs can be substantially enhanced up to 3 times compared to the intrinsic emission of CVD-grown WS_2 flakes. We show that fluorescent enhancement of nanoantenna-coupled 2-D materials unlike quantum dots is an areal average effect rather than a hot-spot-like effect and discuss how the On- and Off-resonance plasmonic of the TMD film's excitonic luminescence is susceptible to electric field intensity variations caused by surface plasmons.

Samples studied here consist of WS_2 monolayer flakes grown directly by CVD on 100 nm of thermal SiO_2 on a Si wafer. The bright-field microscopy image in Figure 1a shows the bare substrate appearing purple, the single-layer material as dark blue, and thicker material regions as lighter blue areas. To characterize our emitter material, micro-Raman, micro-PL, and differential reflectance spectra were taken on WS_2 flakes on a SiO_2/Si substrate at room temperature. We confirm the thickness of the WS_2 material by the appropriate difference in the intensity of the interlayer phonon mode A_{1g} between material identified as multilayer and single-layer (Figure1b) as well as a corresponding difference in PL intensity.[42,43] We further analyze the Raman signal by a multi-Lorentzian fitting of all recognizable features in both monolayer and few-layer WS_2 (Figure 1b). The strongest peak at ~354 cm^{-1} is attributed to the in-plane E_{2g}^1 and second-order vibrational mode 2LA(M), and the peak at ~418 cm^{-1} to the out-of-plane vibrational mode A_{1g}(G). Raman modes derived from density functional theory (DFT) calculations confirm the Raman mode assignment (see Methods). The A_{1g}(G) mode blue shifts and its relative intensity to the in-plane vibrational mode component increases, with an increasing number of WS_2 layers. This is expected due to a stronger interlayer force caused by van der Waals interactions.[43] The emission spectrum of WS_2 shows a dependence on flake thickness: monolayer WS_2 flakes exhibit a drastically increased emission quantum efficiency, indicating the indirect-to-direct band-gap transition upon multilayer to monolayer scaling (Figure 1a).[44]

The PL emission spectrum of a monolayer WS_2 flake is dominated by the *A* exciton peak at 633 nm (~1.96 eV) wavelength. After deposition of an Al_2O_3 spacer layer, the PL emission spectrum of monolayer WS_2 slightly red-shifts from the pristine value of 633 nm (~1.96 eV) to 637 nm (~1.95 eV) (Supporting Information). We attribute this red-shift to a combination of strain imparted by the electron beam evaporation of Al_2O_3 and weak electronic interaction with the Al_2O_3 film. Following the deposition of the antennae, we find an enhancement of the PL emission of monolayer WS_2 flakes. The 75 nm dimer cavity exhibits the largest increase by a factor of 3.2 (2.7) in peak intensity (in integrated PL count) relative to emission of the reference sample (bare monolayer WS_2 flake) at the same excitation power density (Figure 2). In contrast, monomer and dimer antennae with a radius of 200 nm do not substantially alter the PL peak or intensity of monolayer WS_2. We note that some fluctuations of the enhancement values and spectral response shifts can be expected, because the optical properties of the WS_2 monolayer are strongly influenced by the nanoantenna surface plasmon that can alter the effective pumping of WS_2, generation rate of

DOI: 10.1021/acsphotonics.7b00208
ACS Photonics 2017, 4, 1713−1721

electron−hole pairs, and quantum yield of the emitter system, discussed below.

When a quantum emitter interacts with the local fields of an optical antenna, the coupled system has a larger absorption cross-section compared to an isolated emitter, leading to an optical concentration effect that enhances the effective pump intensity. To reveal such far-field cold-cavity effect and to find the resonances for the monomer and dimer nanoantennae, we analytically describe their spectral scattering efficiency and absorption loss response by dividing both the absorption cross-section area and scattering cross-section area of each individual antenna by its geometrical area:

$$Q_{ext} = Q_{scat} + Q_{abs} = \frac{C_{ext}}{C_{geo}} = \frac{C_{scat} + C_{abs}}{C_{geo}} \quad (1)$$

where Q_{ext}, Q_{scat}, Q_{abs} (C_{scat}, C_{abs}) are extinction, scattering, and absorption efficiency (cross-section), respectively. C_{geo} is the geometrical cross-section of the antenna, which depends on its radius. We note that Q_{abs} is a parasitic part of the cold cavity and needs to be minimized, and it should not be evaluated as the emitter absorption where an enhancement is preferred as long as the system operates in the linear regime. The resonance wavelength and scattering cross-section of the monomer antenna are a function of the permittivity of the plasmonic material and the dimensions of the antenna. We have chosen gold for fabrication of our antennae due to its Drude-like response for wavelengths above 600 nm.

Our modeling of the monomer antenna with a 75 nm radius reveals a scattering efficiency of about 1.8 and 6.3 at an excitation wavelength of 532 nm and emission wavelength of ∼640 nm, respectively, in which the emission of the WS_2 is in resonance with the resonance of the cavity (Figure 3b). Since the monomer is electromagnetically a simple dipole under excitation, we observe the expected monotonic resonance red-shift with increasing dimension of the monomer particle (dashed lines), while the discrepancy from a linear trend can be explained by dispersion. The spectral regions and antenna dimensions to avoid absorption losses are (a) near the blue frequencies in the visible and (b) small monomers (<75 nm) (Figure 3a). Further we find that the dimer antennae fall into two categories depending on whether the interparticle distances (i.e., gap) is positive (true dimer) or negative (lumped dimer) (Figure 3c). For the dimer antennae, the radius of each disc is kept at constant values of 75, 100, and 200 nm and the interparticle distance in between them is swept from negative to positive values, where the negative values of the gap represent overlapping dimer discs. Comparing the spectral resonances, we find that the lumped dimers effectively behave as monomers with a metal particle diameter about equal to the total length of the dimer ($r_{dimer} \approx 2 \times r_{monomer}$) (black dashed line, Figure 3d). Although the scattering efficiency of each dimer antenna is less than the scattering efficiency of its corresponding monomer antenna with the same radius, the scattering cross-section is larger (∼2×) relative to that of monomer antennae. As expected, the resonance for dimers with large positive gaps approaches that of the isolated monomer.

Moreover, the emission intensity profile of an emitter in an optical-cavity antenna is governed by

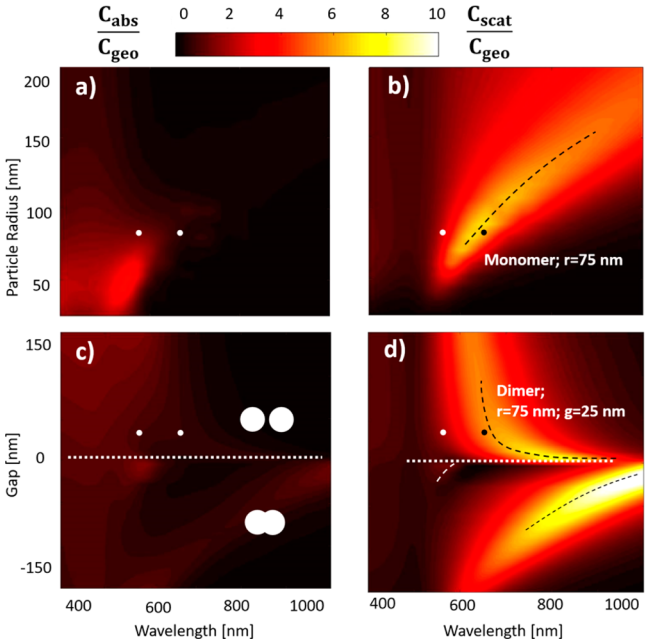

Figure 3. Cold cavity response. Absorption loss (Q_{abs}) (a) and far-field scattering efficiency (Q_{scat}) (b) mapping of monomer nanodisc antennae for a radius range of 50 to 200 nm. (The black and white points represent our fabricated antennae for emission and excitation wavelengths, respectively.) Absorption loss (c) and far-field scattering efficiency (d) for a dimer nanoantenna of single 75 nm radius and in a gap sweeping range from −150 nm (overlapping charge transfer mode) to 150 nm (gap plasmon mode). The points represent our fabricated 75 nm dimer antenna. The scale bar shows the ratio for absorption or scattering cross-section to geometrical cross-section of each type of antenna. The dashed lines are guides to the eye.

$$I_{out} = (I_{pump})_{eff}(\eta_{int})(\eta_{oc}) = \left[I_0 \left(\frac{\iint \frac{|E|^2}{|E_0|^2} ds}{C_{geo}} \right) \right]_{\lambda\text{-Pump}} [F_p \cdot QE]_{\lambda\text{-Emit}} \quad (2)$$

where I_{out} is the outgoing emission from the system, I_{pump} is the effective incoming laser pump intensity onto the monolayer WS_2 emitter, η_{int} is the internal photon generation process of the emitter equal to the spontaneous emission rate enhanced by the Purcell factor, and η_{oc} is the out-coupling efficiency of emitted photons from the monolayer WS_2 via the cavity−antenna system into free space above the sample where the light is collected at the microscope objective, represented here as the quantum efficiency of the antenna.

Regarding the internal photon generation enhancement process of the TMD−cavity system, we focus on the near-field enhancement and Purcell product in eq 2. The overall fluorescence enhancement of monolayer WS_2 by the plasmonic optical antenna can be expressed as the product of excitation rate enhancement, the spontaneous emission probability enhancement (Purcell effect), and the outgoing portion of the spontaneous emission:

$$\frac{I_{out}}{I_0} = \frac{\gamma_{em}}{\gamma_{em}^0} = \frac{\gamma_{exc}}{\gamma_{exc}^0}\frac{\gamma_r}{\gamma_r^0} \quad (3)$$

where the "0" denotes the intrinsic value, γ_{em} is the enhanced and intrinsic fluorescence rate, γ_{exc} is the excitation rate at the

DOI: 10.1021/acsphotonics.7b00208
ACS Photonics 2017, 4, 1713−1721

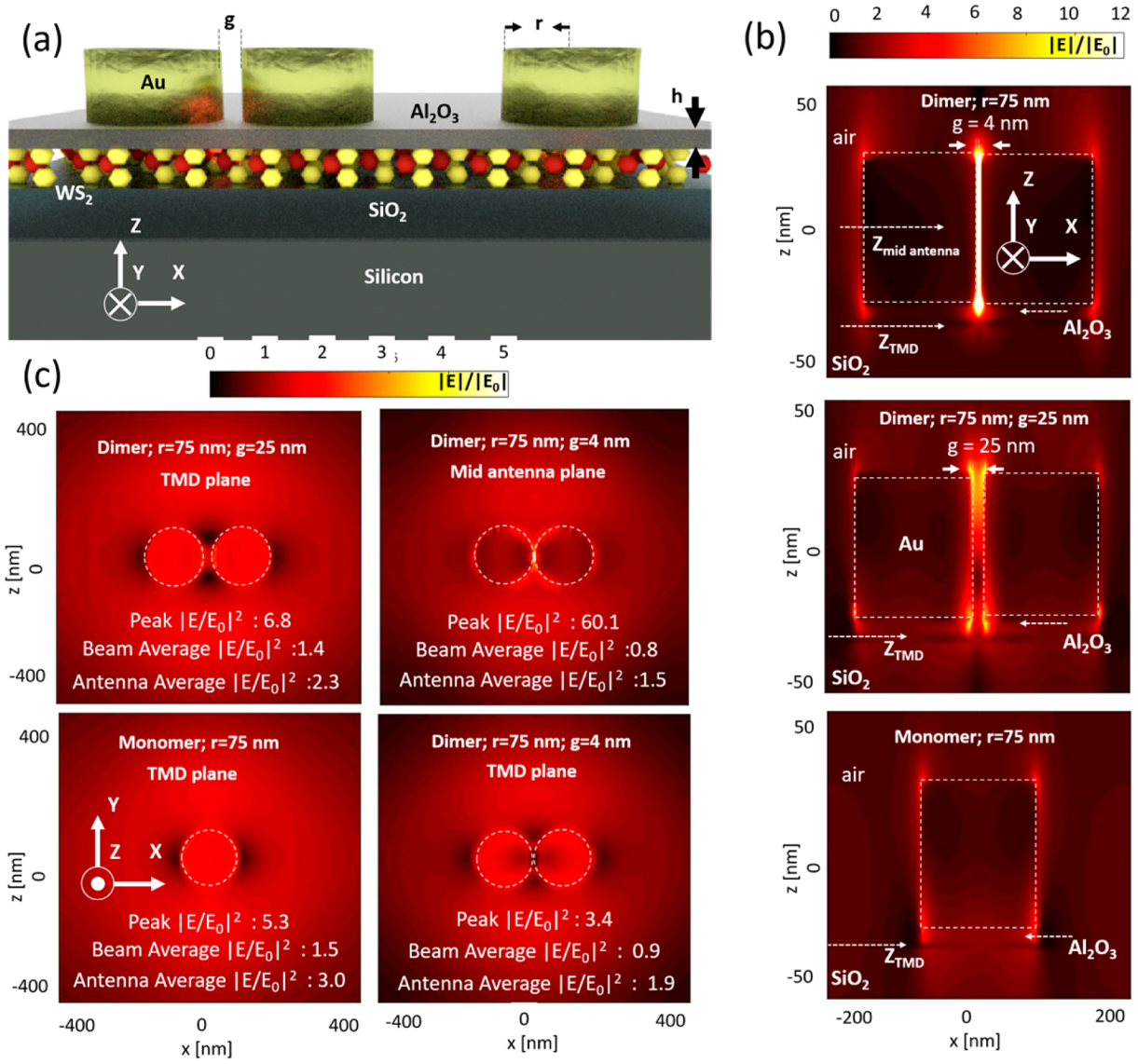

Figure 4. Electric field intensity enhancement ($|E|/|E_0|$) comparison of dimer and monomer antennae showing comparable enhancement at the TMD position, which is separated by a spacer layer to avoid quenching. (a) Schematic of the proposed optical antenna types for PL enhancement of monolayer TMDs. (b) Side view of the electric field intensity magnitude enhancement distribution in a 4 and 25 nm gapped 75 nm radii dimer antenna and a 75 nm radius monomer antenna, respectively, from top to bottom. (c) Comparison of electric field intensity enhancement for the same antennae shown in top view and two different *z*-normal plane positions at the midpoint of the antenna and at the z-normal plane where the TMD layer is positioned. The maximum value, the averaged value over the area of the beam spot size of the simulation, and the averaged value over the area of geometrical antenna cross-section of $(|E|/|E_0|)^2$ is reported for each case.

excitation wavelength of 532 nm, and γ_r is the radiative decay rate of the emitter at an emission wavelength of 640 nm. Since the emitter is excited optically, the excitation rate enhancement is then proportional to the ratio of the squared electric field of the emitter with the optical cavity and without the cavity ($\gamma_{exc}/\gamma^0_{exc} = |E|^2/|E_0|^2$). It is tempting to consider the peak field enhancement of a dimer antenna as the anticipated enhancement of the emission. This is however not an accurate interpretation of the actual experiment; because the spot size of our pump laser is significantly larger than the physical area of the antennae, the excitation and hence the photon generation are not local, hot-spot-like effects, but rather originate from an average across the pump beam radius. In order to obtain (a) an accurate emission enhancement originating from a ~0.8 μm large pump diameter and (b) a complete picture of the nature of the electric field enhancement distribution in the presence of either monomer or dimer antennae, we calculate the spatial distribution of the electromagnetic field profile at the location of the monolayer WS_2 and, for comparison, at the cross-section of the optical antenna for both the excitation and emission wavelengths (Figure 4) (see Methods). The dimer metallic nanoparticles separated by a small gap (4 nm in Figure 4b) support hybridized plasmon resonances because of the capacitive coupling between the plasmon modes of each nanoparticle. Thus, the often-cited high-peak-field enhancement (here 60×) is observed only if a few-atom small point emitter would be positioned precisely inside the gap center (Figure 4c). Even if this is achieved (e.g., using dye molecules), the signal could not be collected from this hot-spot only, because even the highest resolution near-field light collector such as a NSOM averages its signal over an area of hundreds of square nanometers.[46] Since the 2-D TMD cannot be placed

DOI: 10.1021/acsphotonics.7b00208
ACS Photonics 2017, 4, 1713−1721

inside the gap nor right underneath the metal nanoparticle (to avoid quenching), the only logical position would be to place it below or above the antenna, separated by a thin spacer (Figure 4a). Thus, when we measure the field enhancement at the position of a TMD flake residing at an optimized length of 8 nm beneath the metal nanoparticle, the peak field enhancement is only 3.4-fold (Figure 4c). We observe a similar trend for the 100 and 200 nm radius dimer antennae (Supporting Information). It is thus not plausible to simply take the peak intensity as the emission process enhancing value. One can conclude that for nonpoint emitters such as the 2-D WS_2 flake, it becomes necessary to define an averaged excitation field enhancement factor such as by integrating the emission over either the physical area of the antenna,

$$\frac{\gamma_{exc}}{\gamma_{exc}^{0}} = \frac{\iint \frac{|E|^2}{|E_0|^2}\,ds}{S} \tag{4}$$

or, more accurately, over the pump beam area, where S is either the geometrical cross-section of the antenna or the area of the beam. The aforementioned peak intensity inside a small (4 nm) gap dimer of 60 drops to 1.5 (0.8) when averaged over the antenna (beam) area at the unphysical midgap dimer position. For the same antenna, the 3.4× enhancement at the TMD plane underneath the cavity drops to 1.9 (0.9) when averaged over the antenna (beam) (Figure 4c). This shows that no actual excitation rate enhancement is expected for small-gap dimers when TMDs are sitting at a quenching-safe distance away from the antenna. Interestingly, when the gap is increased from 4 nm to 25 nm (as studied here), the average enhancement for the antenna (beam) increases by 21% (53%) compared to the narrower hot-spot gap dimer case. We also note that the monomer with the same radius offers the highest antenna and beam enhancement (Figure 4c, bottom left corner); with the simpler fabrication of monomers over dimers, these results suggest that monomers are equally well-performing to enhance 2D material PL.

A comparison of the far-field (scattering efficiency of disc antenna) and near-field spectra (electric field enhancement) of individual Au nanodiscs (Supporting Information) shows that the far-field scattering efficiency peaks at a larger nanoparticle size than the near-field intensity enhancement. Consequently, one should acknowledge that maximum scattering efficiency is not synonymous with highest near-field enhancement, as claimed also in previous studies.[47−49] Also, often in optics we seek the highest possible quality factor (Q factor) for the highest possible light−matter interaction; but in a high-performing antenna we seek the opposite because we desire radiation losses.[26,49]

Our theoretical near-field and far-field study reveals that the observed PL enhancement of monolayer WS_2 is due to localized electric field and local density of states at both excitation and emission wavelengths, enhancing both the excitation and emission rate (Figure 3, 4). However, since the pump is Stokes-shifted from the emission, an antenna could be designed to enhance either process selectively, provided that the Q's are sufficient for this spectral filtering to occur.

The photon generation rate, here defined as the product between the quantum efficiency and the Purcell factor, is equal to the quantitative radiative decay rate enhancement (γ_r/γ_r^0) (Figure 5b,d):

$$G = \frac{\gamma_r}{\gamma_r^{0}} = F_p \times QE = \left(\frac{\gamma_r}{\gamma_{sp}}\right) \times \left(\frac{\gamma_{sp}}{\gamma_r^{0}}\right) \tag{5}$$

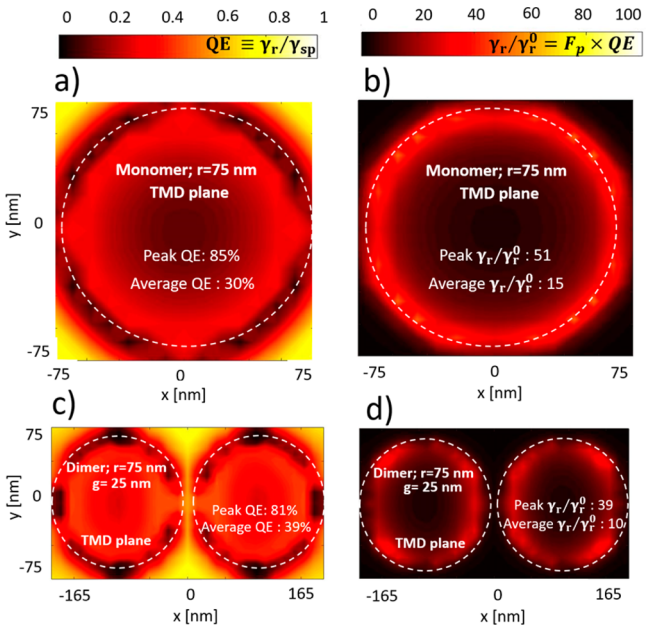

Figure 5. Photon generation rate. Spatial map of the quantum efficiency (a, c) and enhancement in the total radiative rate of $F_p \times QE$ (b, d) for a dipole emitting at a z normal plane corresponding to the position of the TMD in the fabricated device. The dashed white lines represent the position of the dimer antennae.

where γ_{sp} is the spontaneous emission rate of the emitter at an emission wavelength of ∼640 nm, F_p is the Purcell factor, and QE is the quantum efficiency, defined as the portion of spontaneous emission coupled out of the cavity into the free space. We obtain this at the emission wavelength of the monolayer WS_2 (∼640 nm) positioned under a 75 nm radius monomer or dimer nanocavity compared to an as-grown WS_2 flake (Figure 5a,b) (see Methods). The maximum attained generation rate for a dimer of 75 nm radius and 25 nm gap is ∼39 times, and the averaged value over the area underneath the geometrical cross-section of the dimer antenna is about ∼10 times the intrinsic radiative rate (Figure 5d). The QE of the fluorescence process is estimated by the ratio of the radiated power measured in the far-field to the total power injected by the emitter (Figure 5a,c):

$$QE = \frac{\gamma_{rad}}{\gamma_{rad} + \gamma_{loss} + \gamma_{nr}} = \frac{P_{rad}}{P_{rad} + P_{loss}} \tag{6}$$

However, the decay rate of the excitons to nonradiative channels (γ_{nr}) such as phonons is not an EM process and is not captured in our finite-difference time-domain (FDTD) simulation; hence, it is taken as zero. In this approximation, the average QE of the emitter sitting below the dimer cavity is ∼39%.

On the basis of these numerical estimates, we expect PL enhancement over the beam spot (geometrical cross-section) for the 75 nm radius monomer and dimer antenna cavities to be 2.1 (30.0)- and 3.8 (23.0)-fold, respectively. Note the ∼10× reduction as a consequence of the mismatch between beam and optimized antenna size. In order to compare our measurements

DOI: 10.1021/acsphotonics.7b00208
ACS Photonics 2017, 4, 1713−1721

to the modeling, we fit the experimental beam intensity profile to a Gaussian function and take the full width at half-maximum (fwhm) as the beam spot size (Figure 2c). These experimental results corroborate our computational expectations, but show slightly lower values. Another common way of expressing experimental results is to define the normalized experimental enhancement factor ($\langle EF_{exp} \rangle$) as[27]

$$\left\langle EF_{exp} \right\rangle = \frac{I_{cav}}{I_0} / \frac{S_{cav}}{S_0} \tag{7}$$

where S_{cav} is the area of a cavity, S_0 is the area of the Gaussian excitation beam, I_{cav} is the PL intensity from the cavity, and I_0 is the PL intensity from the as-grown WS_2 flake, resulting in an $\langle EF_{exp} \rangle$ of 50.9- and 39.7-fold. This evaluation leads to an overestimation of the local enhancement within the cavity from our experimental result, because per our simulation the electric field intensity and Purcell factor distribution directly under the nanoantenna are significantly larger than the area around the antenna S_{cav}. Consequently, our findings point to the need for an evaluation of the field enhancement over a much larger area than S_{cav} in order to deduce realistic material properties from the cavity experiments.

The shape of the PL spectrum in the cavity is conceptually similar to that of the control sample. However, we observe a spectral narrowing in fwhm value from 16.7 nm to 15.7, 13.5, and 14.6 nm for the cases of the 75 nm radius monomer disc antenna and the 75 and 100 nm radii dimer antennae, respectively. We note that these effects are not sustained for the PL spectrum of the 200 nm radius dimer antenna, for which we observe a red-shift by 3.5 nm (relative to the intrinsic emission spectrum of as-grown WS_2 flakes) and a band broadening to 21.8 nm. We attribute this observation to convolution of the PL emission spectrum of monolayer WS_2 with the fundamental resonance of the 200 nm dimer cavity (Supporting Information). Supporting modeling indicates narrowing of the emission spectrum with the dot radius, so that for the cases of the 75 and 100 nm radii dimers the resonance condition affects narrowing and not broadening of the WS_2 emission peak. This results in a higher quality factor and sharper spectral response (Supporting Information), in line with a prediction based on Wheeler's limit.[50] Our experimental findings highlight that the quality factor of nanoantennae increases as the dimensions of the disc decrease.

In conclusion, we have demonstrated that optical nanoantennae can be used to control the emitting properties of monolayer TMDs. This control was achieved using two types of metallic cavities (monomer vs dimer) at four different sizes. These emission dynamics were also supported by numerical calculations. In particular, we have demonstrated the fluorescent enhancement of 2-D materials, and unlike quantum dots there is an areal average effect that has to be taken into account. We have also observed band narrowing of the emission response when the resonance of the cavity corresponds to the emission wavelength of monolayer WS_2. Both monomer and dimer nanoantenna architectures are scalable to emission resonances of other members of the TMD family as well including $MoTe_2$, which emits at a telecommunication wavelength in the near-infrared. The demonstrated nanoantenna-controlled emission from a monolayer WS_2 flake could open a pathway to visible light sources based on lithographically fabricated nanoantennae supporting a variety of optoelectronic applications.[51−56]

METHODS

Growth Method. Single- and multilayer tungsten disulfide (WS_2) was grown via ambient-pressure chemical vapor deposition utilizing a tube furnace. The process is a variation of our previously published work on transition metal dichalcogenide materials.[57−59] The reagents were ammonia meta tungstate (AMT) and elemental sulfur. The process starts by spin-coating a 3.1 mmol aqueous solution of AMT onto a SiO_2/Si substrate. The resultant residue serves as the tungsten source for our CVD growth. We place a target substrate directly face-down onto this source substrate and insert this stack into the growth region at the center of the process tube in our tube furnace. An alumina boat containing elemental sulfur is placed inside the process tube far enough upstream of the furnace heating coil so that it just fully melts when the furnace center reaches the peak growth temperature of 850 °C.

The temperature ramp for WS_2 growth commences after a nitrogen purge of the process tube for 15 min at 5 scfh. After that we ramp the furnace to 500 °C to decompose the AMT into tungsten trioxide, releasing water and ammonia vapor. After 20 min the reaction is complete, and we ramp up to the growth temperature of 850 °C and remain there for 15 min. Subsequently, the furnace is allowed to cool naturally to 200 °C before the process tube is opened to air and the target substrate retrieved.

Fabrication Method. After WS_2 films were deposited, a ∼8 nm layer of aluminum oxide (Al_2O_3) was deposited onto the sample as a spacer between the emitter and the plasmonic antennae. Next, we fabricated monomer and dimer optical disk antennae, varying the diameters and gaps, onto the large-area WS_2 film using electron beam lithography. We then followed with gold deposition using electron beam evaporation. Finally the gold film is lifted off using a PG remover. Lithographical fabrication of the antennae allows for control over dimensions and position of particles, permitting us to tune the plasmonic resonance of each antenna element. The nanoantenna were arranged at a center-to-center distance of 4 μm to prevent interference of absorption cross-sections of individual antennae (Supporting Information).

Raman and Photoluminescence Spectroscopy. Raman and PL spectroscopy were performed using a custom-built spectrometer equipped with a 532 nm excitation laser and a CCD detector (Supporting Information). The nonlinear emission spectra were acquired in reflection geometry to a spectrometer including a 532 nm notch filter to reject the pump wavelengths. The spectrometer acquisition parameters were held constant and set to ensure high signal-to-noise ratio for the weakest signal. All measurements were performed in air at ∼25 °C and atmospheric pressure.

Reflectance Spectroscopy. Reflectance measurements were performed using a 20 W halogen light source by measuring the difference in reflected intensity from the WS_2/SiO_2 and bare silicon wafer substrate and normalizing this to the substrate-reflected intensity. For optical microscopy, we used white light and a 100× objective lens.

FDTD Calculation Method. Reflectance, in-plane and out-of-plane electric field intensities, Purcell factor, scattering, and absorption spectra were calculated. Optical constants of WS_2 were obtained from Liu et al.[60] The refractive indexes of silica, silicon, alumina, and gold were used directly from Palik as well as Johnson and Christy.[61,62]

DOI: 10.1021/acsphotonics.7b00208
ACS Photonics 2017, 4, 1713−1721

We used the Lumerical three-dimensional FDTD solver for all Maxwell equation calculations. For scattering effect calculations, we employed a total field scattered field (TFSF) method. The plane wave was launched normally from the top of monomer or dimer antennae. Two (virtual) power-flow monitors (six detectors each) were positioned inside and outside the TFSF source, surrounding the antenna, to measure the absorption and scattering cross sections, in order. The power flow analysis calculates the net absorbed power and scattered power from the particle. For Purcell factor calculations, a dipole source was used (Supporting Information). In all other problems, a normal incident broadband plane wave was implemented. To ensure that scattered light does not return to the simulation region, a perfect matching layer was applied as boundary condition in all directions.

For Purcell factor and quantum efficiency calculations, we sampled the plane at the level of the 2-D TMD sheet with a dipole source. We calculated the radiated power by a set of (virtual) field power monitors as one transmission box surrounding only the dipole source and another transmission box far away from the source but surrounding both the emitter and cavity. The expression deployed in this method to evaluate the Purcell factor is F_p = emitted-power (f)/source-power (f), where f is the optical frequency. The source-power returns the power that the dipole would radiate in a homogeneous material. The emitted-power is the power transmitted out of a boxed area surrounding the dipole source due to the dispersive materials used in the cavity.

■ ASSOCIATED CONTENT

Supporting Information

The Supporting Information is available free of charge on the ACS Publications website at DOI: 10.1021/acsphotonics.7b00208.

Description of near-field intensity distribution, scattering efficiency, absorption loss map, and quality factor for all dimer antennae; additional Purcell factor results for a narrow gap dimer antenna; nanoantenna fabrication steps and SEM images; PL measurement setup; DFT calculation results (PDF)

■ AUTHOR INFORMATION

Corresponding Author

*E-mail: tahersima@gwu.edu.

ORCID

Mohammad H. Tahersima: 0000-0001-6759-8869
M. Danang Birowosuto: 0000-0002-9997-6841
Volker J. Sorger: 0000-0002-5152-4766

Notes

The authors declare no competing financial interest.

■ ACKNOWLEDGMENTS

We thank the National Science Foundation and the Materials Genome Initiative for support under the award number NSF DMREF 14363300/1455050 and NSF EAPSI 1613966. V.S. is supported by the Air Force Office of Scientific Research Young Investigator Program under grants FA9550-14-1-0215 and FA9550-14-1-0378.

■ REFERENCES

(1) Mak, K. F.; Lee, C.; Hone, J.; Shan, J.; Heinz, T. F. Atomically Thin MoS2: A New Direct-Gap Semiconductor. *Phys. Rev. Lett.* **2010**, *105*, 136805.

(2) Splendiani, A.; Sun, L.; Zhang, Y.; Li, T.; Kim, J.; Chim, C. Y.; Galli, G.; Wang, F. Emerging Photoluminescence in Monolayer MoS2. *Nano Lett.* **2010**, *10*, 1271−1275.

(3) Gutiérrez, H. R.; Perea-López, N.; Elías, A. L.; Berkdemir, A.; Wang, B.; Lv, R.; López-Urías, F.; Crespi, V. H.; Terrones, H.; Terrones, M. Extraordinary Room-Temperature Photoluminescence in Triangular WS2Monolayers. *Nano Lett.* **2013**, *13*, 3447−3454.

(4) Peimyoo, N.; Shang, J.; Cong, C.; Shen, X.; Wu, X.; Yeow, E. K. L.; Yu, T. Nonblinking, Intense Two-Dimensional Light Emitter: Monolayer WS2 Triangles. *ACS Nano* **2013**, *7*, 10985−10994.

(5) Xia, F.; Wang, H.; Xiao, D.; Dubey, M.; Ramasubramaniam, A. Two-dimensional material nanophotonics. *Nat. Photonics* **2014**, *8*, 899−907.

(6) Tahersima, M. H.; Sorger, V. J. Enhanced photon absorption in spiral nanostructured solar cells using layered 2D materials. *Nanotechnology* **2015**, *26*, 344005.

(7) Ma, Z.; Tahersima, M. H.; Khan, S.; Sorger, V. J. Two-Dimensional Material-Based Mode Confinement Engineering in Electro-Optic Modulators. *IEEE J. Sel. Top. Quantum Electron.* **2017**, *23*, 81−88.

(8) Britnell, L.; et al. Strong light−matter interactions in heterostructures of atomically thin films. *Science* **2013**, *340*, 1311−1314.

(9) Lopez-Sanchez, O.; Lembke, D.; Kayci, M.; Radenovic, A.; Kis, A. Ultrasensitive photodetectors based on monolayer MoS2. *Nat. Nanotechnol.* **2013**, *8*, 497−501.

(10) Cheng, R.; et al. Electroluminescence and photocurrent generation from atomically sharp WSe2/MoS2 heterojunction p−n diodes. *Nano Lett.* **2014**, *14*, 5590−5597.

(11) Yang, W.; et al. Electrically Tunable Valley-Light Emitting Diode (vLED) Based on CVD-Grown Monolayer WS2. *Nano Lett.* **2016**, *16*, 1560−1567.

(12) Mak, K. F.; He, K.; Lee, C.; Lee, G. H.; Hone, J.; Heinz, T. F.; Shan, J. Tightly bound trions in monolayer MoS2. *Nat. Mater.* **2013**, *12*, 207−211.

(13) Wang, Z.; Zhao, L.; Mak, K. F.; Shan, J. Probing the Spin-Polarized Electronic Band Structure in Monolayer Transition Metal Dichalcogenides by Optical Spectroscopy. *Nano Lett.* **2017**, *17*, 740−746.

(14) Shang, J.; Shen, X.; Cong, C.; Peimyoo, N.; Cao, B.; Eginligil, M.; Yu, T. Observation of Excitonic Fine Structure in a 2D Transition-Metal Dichalcogenide Semiconductor. *ACS Nano* **2015**, *9*, 647−655.

(15) Wang, X. H.; Ning, J. Q.; Su, Z. C.; Zheng, C. C.; Zhu, B. R.; Xie, L.; Wu, H. S.; Xu, S. J. Photoinduced doping and photoluminescence signature in an exfoliated WS2 monolayer semiconductor. *RSC Adv.* **2016**, *6*, 27677−27681.

(16) Chernikov, L.; Berkelbach, T. C.; Hill, H. M.; Rigosi, A.; Li, Y.; Aslan, O. B.; Reichman, D. R.; Hybertsen, M. S.; Heinz, T. F. Exciton Binding Energy and Nonhydrogenic Rydberg Series in Monolayer WS2. *Phys. Rev. Lett.* **2014**, *113*, 076802.

(17) Plechinger, G.; Nagler, P.; Kraus, J.; Paradiso, N.; Strunk, C.; Schüller, C.; Korn, T. Identification of excitons, trions and biexcitons in single-layer WS2. *Phys. Status Solidi RRL* **2015**, *9*, 457−461.

(18) You, Y.; Zhang, X.; Berkelbach, T. C.; Hybertsen, M. S.; Reichman, D. R.; Heinz, T. F. Observation of biexcitons in monolayer WSe2. *Nat. Phys.* **2015**, *11*, 477−481.

(19) Ye, Z.; Cao, T.; O'Brien, K.; Zhu, H.; Yin, X.; Wang, Y.; Louie, S. G.; Zhang, X. Probing excitonic dark states in single-layer tungsten disulphide. *Nature* **2014**, *513*, 214−218.

(20) Gan, X.; Gao, Y.; Mak, K. F.; Yao, X.; Shiue, R. J.; Zande, A.; Trusheim, M.; Hatami, F.; Heinz, T. F.; Hone, J.; Englund, D. Controlling the spontaneous emission rate of monolayer MoS2 in a photonic crystal nanocavity. *Appl. Phys. Lett.* **2013**, *103*, 181119.

(21) Ye, Y.; Wong, Z. J.; Lu, X.; Ni, X.; Zhu, H.; Chen, X.; Wang, Y.; Zhang, X. Monolayer excitonic laser. *Nat. Photonics* **2015**, *9*, 733−737.

DOI: 10.1021/acsphotonics.7b00208
ACS Photonics 2017, 4, 1713−1721

(22) Taghinejad, H.; Taghinejad, M.; Tarasov, A.; Tsai, M. Y.; Hosseinnia, A. H.; Moradinejad, H.; Campbell, P. M.; Eftekhar, A. A.; Vogel, E. M.; Adibi, A. Resonant Light-Induced Heating in Hybrid Cavity-Coupled 2D Transition-Metal Dichalcogenides. *ACS Photonics* **2016**, *3*, 700−707.
(23) Mukherjee, B.; Kaushik, N.; Tripathi, R. P. N.; Joseph, A. M.; Mohapatra, P. K.; Dhar, S.; Singh, B. P.; Kumar, G. V. P.; Simsek, E.; Lodha, S. Exciton Emission Intensity Modulation of Monolayer MoS2 via Au Plasmon Coupling. *Sci. Rep.* **2017**, *7*, No. 41175.
(24) Taghinejad, H.; Shams-Mousavi, S. H.; Gong, Y.; Taghinejad, M.; Eftekhar, A. A.; Ajayan, P.; Adibi, A. Lattice Plasmon Induced Large Enhancement of Excitonic Emission in Monolayer Metal Dichalcogenides. *Plasmonics* **2016**10.1007/s11468-016-0470-4.
(25) Purcell, E. M.; Torrey, H. C.; Pound, R. V. *Phys. Rev.* **1946**, *69*, 37.
(26) Eggleston, M. S.; Messer, K.; Zhang, L.; Yablonovitch, E.; Wu, M. C. Optical antenna enhanced spontaneous emission. *Proc. Natl. Acad. Sci. U. S. A.* **2015**, *112*, 1704−1709.
(27) Akselrod, G. M.; Ming, T.; Argyropoulos, C.; Hoang, T. B.; Lin, Y.; Ling, X.; Smith, D. R.; Kong, J.; Mikkelsen, M. H. Leveraging Nanocavity Harmonics for Control of Optical Processes in 2D Semiconductors. *Nano Lett.* **2015**, *15*, 3578−3584.
(28) Butun, S.; Tongay, S.; Aydin, K. Enhanced Light Emission from Large-Area Monolayer MoS2 Using Plasmonic Nanodisc Arrays. *Nano Lett.* **2015**, *15*, 2700−2704.
(29) Kern, J.; Trügler, A.; Niehues, I.; Ewering, J.; Schmidt, R.; Schneider, R.; Najmaei, S.; George, A.; Zhang, J.; Lou, J.; Hohenester, U.; Vasconcellos, S. M.; Bratschitsch, R. Nanoantenna-Enhanced Light−Matter Interaction in Atomically Thin WS2. *ACS Photonics* **2015**, *2*, 1260−1265.
(30) Lee, B.; Park, J.; Han, G. H.; Ee, H. S.; Naylor, C. H.; Liu, W.; Johnson, A. T. C.; Agarwal, R. Fano Resonance and Spectrally Modified Photoluminescence Enhancement in Monolayer MoS2 Integrated with Plasmonic Nanoantenna Array. *Nano Lett.* **2015**, *15*, 3646−3653.
(31) Liu, W.; Lee, B.; Naylor, C. H.; Ee, H. S.; Park, J.; Johnson, A. T. C.; Agarwal, R. Strong exciton-plasmon coupling in MoS2 coupled with plasmonic lattice. *Nano Lett.* **2016**, *16*, 1262−1269.
(32) Eggleston, M.; Desai, S.; Messer, K.; Madhvapathy, S.; Xiao, J.; Zhang, X.; Yablonovitch, E.; Javey, A.; Wu, M. C. Enhanced Spontaneous Emission from an Optical Antenna Coupled WSe_2 Monolayer. *Technol. Dig. Ser. - Opt. Soc. Am.* **2015**, DOI: 10.1364/CLEO_QELS.2015.FTu1E.5.
(33) Najmaei, S.; Mlayah, A.; Arbouet, A.; Girard, C.; Leotin, J.; Lou, J. Plasmonic Pumping of Excitonic Photoluminescence in Hybrid MoS2-Au Nanostructures. *ACS Nano* **2014**, *8*, 12682−12689.
(34) Bhanu, U.; Islam, M. R.; Tetard, L.; Khondaker, S. I. Photoluminescence Quenching in Gold MoS2 Hybrid Nanoflakes. *Sci. Rep.* **2015**, *4*, 5575.
(35) Zhu, Z.; et al. Excitonic Resonant Emission−Absorption of Surface Plasmons in Transition Metal Dichalcogenides for Chip-Level Electronic−Photonic Integrated Circuits. *ACS Photonics* **2016**, *3*, 869−874.
(36) Anger, P.; Bharadwaj, P.; Novotny, L. Enhancement and quenching of single-molecule fluorescence. *Phys. Rev. Lett.* **2016**, *96*, 3−6.
(37) Cho, C. H.; Aspetti, C. O.; Turk, M. E.; Kikkawa, J. M.; Nam, S. W.; Agarwal, R. Tailoring hot-exciton emission and lifetimes in semiconducting nanowires via whispering-gallery nanocavity plasmons. *Nat. Mater.* **2011**, *10*, 669−675.
(38) Sorger, V. J.; Pholchai, N.; Cubukcu, E.; Oulton, R. F.; Kolchin, P.; Borschel, C.; Gnauck, M.; Ronning, C.; Zhang, X. Strongly Enhanced Molecular Fluorescence inside a Nanoscale Waveguide Gap. *Nano Lett.* **2011**, *11*, 4907−4911.
(39) Chen, H.; Yang, J.; Rusak, E.; Straubel, J.; Guo, R.; Myint, Y. W.; Pei, J.; Decker, M.; Rockstuhl, C.; Lu, Y.; Kivshar, Y. S.; Neshev, D. Manipulation of photoluminescence of two-dimensional MoSe2 by gold nanoantennas. *Sci. Rep.* **2016**, *6*, 22296.
(40) Sobhani, A.; Lauchner, A.; Najmaei, S.; Ayala-Orozco, C.; Wen, F.; Lou, J.; Halas, N. J. Enhancing the photocurrent and photoluminescence of single crystal monolayer MoS2 with resonant plasmonic nanoshells. *Appl. Phys. Lett.* **2014**, *104*, 031112.
(41) Cui, Y.; et al. High-Performance Monolayer WS2 Field-Effect Transistors on High-κ Dielectrics. *Adv. Mater.* **2015**, *27*, 5230−5234.
(42) Wang, X. H.; Ning, J. Q.; Zheng, C. C.; Zhu, B. R.; Xie, L.; Wu, H. S.; Xu, S. J. Photoluminescence and Raman mapping characterization of WS_2 monolayers prepared using top-down and bottom-up methods. *J. Mater. Chem. C* **2015**, *3*, 2589−2592.
(43) Berkdemir, A.; et al. Identification of individual and few layers of WS_2 using Raman Spectroscopy. *Sci. Rep.* **2013**, *3*, 1755.
(44) Zhao, W.; Ghorannevis, Z.; Chu, L.; Toh, M.; Kloc, C.; Tan, P.-H.; Eda, G. Evolution of Electronic Structure in Atomically Thin Sheets of WS_2 and WSe_2. *ACS Nano* **2013**, *7*, 791−797.
(45) Lee, Y.-H.; Zhang, X.-Q.; Zhang, W.; Chang, M.-T.; Lin, C.-T.; Chang, K.-D.; Yu, Y.-C.; Wang, J. T.-W.; Chang, C.-S.; Li, L.-J.; Lin, T.-W. Synthesis of Large-Area MoS 2 Atomic Layers with Chemical Vapor Deposition. *Adv. Mater.* **2012**, *24*, 2320−2325.
(46) Oshikane, Y.; Kataoka, T.; Okuda, M.; Hara, S.; Inoue, H.; Nakano, M. Observation of nanostructure by scanning near-field optical microscope with small sphere probe. *Sci. Technol. Adv. Mater.* **2007**, *8*, 18110.1016/j.stam.2007.02.013
(47) Yan, B.; Boriskina, S. V.; Reinhard, B. M. Design and Implementation of Noble Metal Nanoparticle Cluster Arrays for Plasmon Enhanced Biosensing. *J. Phys. Chem. C* **2011**, *115* (50), 24437−24453.
(48) Biagioni, P.; Huang, J. S.; Hecht, B. Nanoantennas for Visible and Infrared Radiation. *Rep. Prog. Phys.* **2012**, *75*, 024402.
(49) Bonakdar, A.; Mohseni, H. Impact of optical antennas on active optoelectronic devices. *Nanoscale* **2014**, *6*, 10961.
(50) Wheeler, H. Small antennas. *IRE Trans. Antennas Propag.* **1975**, *AP-24*, 462−469.
(51) Li, N.; Liu, K.; Sadana, D. K.; Sorger, V. J. Nano III-V Plasmonic Light-Sources for Monolithic Integration on Silicon. *Sci. Rep.* **2015**, *5*, 14067.
(52) Liu, K.; Li, N.; Sadana, D. K.; Sorger, V. J. Integrated nanocavity plasmon light-sources for on-chip optical interconnects. *ACS Photonics* **2016**, *3*, 233−242.
(53) Fratalocchi, A.; Dodson, C. M.; Zia, R.; Genevet, P.; Verhagen, E.; Altug, H.; Sorger, V. J Nano-optics gets practical: Plasmon Modulators. *Nat. Nanotechnol.* **2015**, *10*, 11−15.
(54) Birowosuto, M. D.; Takiguchi, M.; Olivier, A.; Tobing, L. Y.; Kuramochi, E.; Yokoo, A.; Hong, W.; Notomi, M. *Opt. Commun.* **2017**, *383*, 555−560.
(55) Ye, C.; Liu, K.; Soref, R.; Sorger, V. J. 3-Waveguide 2 × 2 Plasmonic Electro-optic Switch. *Nanophotonics* **2015**, *4* (1), 261−268.
(56) Sun, S.; Badaway, A.; Narayana, V.; El-Ghazawi, T.; Sorger, V. J. Photonic-Plasmonic Hybrid Interconnects: Efficient Links with Low latency, Energy and Footprint. *IEEE Photonics J.* **2015**, *7*, 6.
(57) Mann, J.; Sun, D.; Ma, Q.; Preciado, E.; Yamaguchi, K.; Chen, J.-R.; Heinz, T. F.; Kawakami, R.; Bartels, L. Facile Growth of Sub-Millimeter Scale Monolayer MoS2 Films on SiO2/Si. *Eur. Phys. J. B* **2013**, *86*, 226.
(58) Tanabe, I.; et al. Band structure characterization of WS2 grown by chemical vapor deposition. *Appl. Phys. Lett.* **2016**, *108*, 252103.
(59) Mann, J.; et al. 2-Dimensional Transition Metal Dichalcogenides with Tunable Direct Band Gaps: MoS2(1-x)Se2x Monolayers. *Adv. Mater.* **2014**, *26*, 1399−1404.
(60) Liu, H. L.; Shen, C. C.; Su, S. H.; Hsu, C.-L.; Li, M. Y.; Li, L. J. Optical properties of monolayer transition metal dichalcogenides probed by spectroscopic ellipsometry. *Appl. Phys. Lett.* **2014**, *105*, 201905.
(61) Palik, E. D. *Handbook of Optical Constants of Solids*; Academic Press: Waltham, MA, 1998; Vol. 3.
(62) Johnson, P. B.; Christy, R. W. Optical Constants of the Noble Metals. *Phys. Rev. B* **1972**, *6*, 4370.

DOI: 10.1021/acsphotonics.7b00208
ACS Photonics 2017, 4, 1713−1721